

## Generalized geometrical scaling behavior of elastic hadron-hadron scattering amplitudes at high energies

M. Kawasaki

*Physics Department, Gifu University, Yanagido, Gifu 501-11, Japan*

T. Maehara

*Faculty of School Education, Hiroshima University, Hiroshima 734, Japan*

M. Yonezawa

*Department of Physics, Hiroshima University, Higashi-Hiroshima 724, Japan*

(Received 12 February 1993)

A detailed comparison of the generalized geometrical scaling (GGS) hypothesis for elastic hadron-hadron scattering amplitudes is made with the measurements of differential cross sections of  $pp$  and  $\bar{p}p$  scattering as well as  $\pi^{\pm}p$  and  $K^{\pm}p$  scattering at high energies. The GGS predictions for  $pp$  and  $\bar{p}p$  scattering show good agreement with the experiments in the energy range from the CERN Intersecting Storage Ring to the Fermilab Tevatron collider ( $\sqrt{s} = 20\text{--}1800$  GeV). In the region below 20 GeV, where we also analyze  $\pi^{\pm}p$  and  $K^{\pm}p$  scattering, we observe GGS behavior down to  $\sim 10$  GeV, especially for  $pp$  scattering.

PACS number(s): 13.85.Dz, 12.40.Pp

### I. INTRODUCTION

The geometrical scaling (GS) model for elastic hadron-hadron diffractive scattering [1] was motivated by the success of the scaling for multiplicity distributions in inelastic reactions proposed by Koba, Nielsen, and Olesen [2]. Theoretically GS can be proved as an asymptotic behavior under some generally accepted conditions, if the total cross section rises as  $\ln^2(s)$  in the high-energy limit  $s \rightarrow \infty$  [3]. Experimentally GS has shown its partial success: the measured differential cross sections of  $pp$  scattering at the CERN Intersecting Storage Ring (ISR) have exhibited such a feature [4]. Subsequent experiments of  $\bar{p}p$  scattering at higher energies, however, show the increase of the elasticity [5] which invalidates this hypothesis.

If the GS behavior observed for the  $pp$  experiments at ISR energies is not accidental, the existence of a more general underlying property, not confined to the asymptotic region, of diffractive interaction is reasonably suspected behind it. In order to investigate this possibility, we previously examined a generalization of geometrical scaling hypothesis and have shown that this generalized geometrical scaling (GGS) gives a unified explanation of behaviors of  $pp$  and  $\bar{p}p$  scattering in the energy region from the CERN ISR to the Fermilab Tevatron collider [6].

In the previous analysis we tentatively assumed the “dipole”-type eikonal for simplicity as in the Chou-Yang model [7]. In the geometrical picture of the diffractive interaction of the Chou-Yang model with modification by Durand and Lipen [8], the eikonal for scattering of hadron  $A$  and hadron  $B$  is assumed to be proportional to the convolution of the matter distributions of  $A$  and  $B$ , for

which the dipole electromagnetic form factor is taken in the case of the proton. This choice seems to be very natural in the framework of the factorized eikonal (FE) model of the geometrical picture [9]. If the scaling exists, however, the relation between the eikonal and the matter distribution of hadron seems less obvious, and, therefore, we have no strong reason to adhere to the “dipole” form of the eikonal. Further the “dipole” does not explain well the  $pp$  differential cross sections at large momentum transfers even at ISR energies. The purpose of this work is to give a detailed account of predictions of GGS to each of  $pp$  and  $\bar{p}p$  scattering as well as to  $\pi^{\pm}p$  and  $K^{\pm}p$  scattering by using eikonal which is determined to reproduce the experimental data at a specific energy for each process.

### II. GENERALIZED GEOMETRICAL SCALING

Neglecting spin effects, we write the c.m. system (c.m.s.) scattering amplitude as

$$f(s, t) = \text{Re}f(s, t) + i \text{Im}f(s, t), \quad (1)$$

with the normalization of the amplitude as

$$\frac{d\sigma}{dt} = \frac{\pi}{k^2} ([\text{Re}f]^2 + [\text{Im}f]^2). \quad (2)$$

In the impact-parameter representation the imaginary part is assumed to be given in terms of the real eikonal  $\Omega(s, b)$  as

$$\text{Im}f(s, t) = k \int_0^{\infty} b db \{1 - e^{-\Omega(s, b)}\} J_0(\sqrt{-t} b), \quad (3)$$

and the real part is introduced tentatively by the Martin formula [10]

$$\text{Re}f(s,t) = \rho \frac{d}{dt} [t \text{Im}f(s,t)] . \quad (4)$$

Here  $k$  is the c.m.s. momentum,  $t$  the squared momentum transfer,  $b$  the impact parameter,  $J_0$  the cylindrical Bessel function of the order zero, and  $\rho$  the ratio of the real part to the imaginary part of the forward-scattering amplitude.

We assume that  $\Omega(s,b)$  is factorized as [11]

$$\Omega(s,b) = w(s)g(b/r(s)) , \quad (5)$$

where  $w$  and  $r$  are functions depending only on  $s$  and should be taken to reproduce *both* the total ( $\sigma_t$ ) and the elastic cross section ( $\sigma_{el}$ ).

For  $\sigma_t$  and  $\sigma_{el}$  we have

$$\begin{aligned} \sigma_t &= 4\pi \int_0^\infty bdb [1 - e^{-w(s)g(b/r(s))}] \\ &= 4\pi r^2 \int_0^\infty \beta d\beta a(\beta) \end{aligned} \quad (6)$$

and

$$\begin{aligned} \sigma_{el} &= 2\pi \int_0^\infty bdb [1 - e^{-w(s)g(b/r(s))}]^2 \\ &\quad + \pi \int_{-\infty}^0 dt [\text{Re}f(s,t)]^2 \\ &= 2\pi r^2 \int_0^\infty \beta d\beta [a(\beta)]^2 + \pi \int_{-\infty}^0 dt [\text{Re}f(s,t)]^2 \end{aligned} \quad (7)$$

with

$$a(\beta) = 1 - e^{-w(s)g(\beta)} .$$

We now define the imaginary-part elasticity  $x_I$  by the contribution of the imaginary part of the scattering amplitude to the elastic cross section, i.e., the contribution from the first term on the right-hand side of Eq. (7), which is denoted by  $\sigma_{el}^I$  [12]. Then,  $x_I$  is independent of the scaling length parameter  $r$ , and the strength function  $w$  is uniquely determined by  $x_I$ . In this sense  $w$  is a function of  $x_I$  and we write

$$w(s) = h(x_I(s); g) . \quad (8)$$

For the value of  $w$  fixed for a given  $x_I$ , the scaling parameter  $r$  is fixed to give  $\sigma_t$ . Hence from Eq. (6) we have the equation

$$r(s) = \sqrt{\sigma_t(s) / \kappa(x_I(s); g)} , \quad (9)$$

where

$$\kappa(x_I; g) \equiv 4\pi \int_0^\infty \beta d\beta [1 - e^{-h(x_I; g)g(\beta)}] . \quad (10)$$

This implies that only the scaling satisfying Eq. (9) works consistently. The GS hypothesis [1] assumes  $r(s) \propto \sqrt{\sigma_t(s)}$  and  $w(s) = \text{const}$ , while the FE model [9] is given by  $r(s) = \text{const}$ .

Here we note that, if the real part is given by the Martin formula (4), its contribution to the elastic cross sec-

tion is written by

$$\pi \int_{-\infty}^0 dt [\text{Re}f(s,t)]^2 = \frac{\rho^2}{2} \pi r^2 \int_0^\infty \beta d\beta \left[ \beta \frac{d}{d\beta} a(\beta) \right]^2 ,$$

which also scales as that of the imaginary part.

The scaling behavior of the scattering amplitude is completely specified by the functional form of  $g(\beta)$ . The problem is, then, whether or not there exists  $g(\beta)$  such as reproducing measured elastic differential cross sections. Previously we have taken  $g(\beta) = \frac{1}{8} \beta^3 K_3(\beta)$  [ $K_3(\beta)$  is the modified Bessel function of the order 3] [6], which is the Fourier-Bessel transform of the square of the dipole form factor,  $1/(1-t/\mu^2)^2$  ( $\beta = \mu b$ ) [7,8]. We call this case ‘‘dipole,’’ though it may be somewhat misleading. This ‘‘dipole’’ form of the eikonal explains the measurements of  $pp$  and  $\bar{p}p$  at  $-t \leq 1.5$  (GeV/c)<sup>2</sup> in the energy region of the CERN ISR [13–20], the CERN Super Proton Synchrotron (SPS) [21], and the Fermilab Tevatron collider [22] ( $\sqrt{s} = 20$ –1800 GeV).

This eikonal, however, does not explain the measured differential cross sections of  $pp$  and  $\bar{p}p$  at ISR energies at the bump and beyond: the predicted cross section decreases faster with increasing  $-t$  than the measurements. If we examine more closely, the predicted position of the first dip seems to be smaller than the measurements. It is, therefore, desirable, to use an eikonal which better reproduces the  $pp$  and  $\bar{p}p$  data than the ‘‘dipole’’ at all the momentum-transfer region of the measurements. If we are concerned with the present experimental data of  $\bar{p}p$  scattering at  $\sqrt{s} = 546$  and 1800 GeV measured only at the small  $-t$  region, the behavior of the scattering amplitude at large momentum transfers will be found to bring little difficulty. In order to establish the proposed generalized scaling hypothesis, however, the experimental test covering large momentum transfers is necessary.

### III. DETERMINATION OF THE EIKONAL

Now we determine the form of the eikonal covering the momentum-transfer range as wide as possible. For  $pp$  and  $\bar{p}p$  scattering, this was done by using the data of  $pp$  scattering at laboratory momentum  $p_L = 200$  GeV/c ( $\sqrt{s} = 19.4$  GeV), where the experiments were performed at the range of momentum transfer  $-t \leq 12$  (GeV/c)<sup>2</sup> [23,24]. For this purpose we use an expression [25] for the imaginary part of the scattering amplitude:

$$\text{Im}f(s,t) = kA \left[ 1 - \frac{t}{t_1} \right] \left[ 1 - \frac{t}{t_2} \right] \left[ 1 - \frac{t}{\lambda^2} \right]^{-n} . \quad (11)$$

By taking the Fourier-Bessel transform of the amplitude (11), we have the following expression for the eikonal from Eq. (3):

$$\begin{aligned} 1 - e^{-\Omega(s,b)} &= \frac{A \lambda^6}{t_1 t_2} \frac{(\lambda b)^{n-3}}{2^{n-3}(n-3)!} \left[ K_{n-3}(\lambda b) - \left[ 2 - \frac{t_1 + t_2}{\lambda^2} \right] \frac{\lambda b}{2(n-2)} K_{n-2}(\lambda b) \right. \\ &\quad \left. + \left[ 1 - \frac{t_1}{\lambda^2} \right] \left[ 1 - \frac{t_2}{\lambda^2} \right] \frac{(\lambda b)^2}{2^2(n-1)(n-2)} K_{n-1}(\lambda b) \right] , \end{aligned} \quad (12)$$

TABLE I. Values of parameters of the imaginary parts of the scattering amplitudes in Eq. (11) determined from the experiments of  $pp$  scattering at  $p_L=200$  GeV/c,  $\pi^-p$  scattering at 200 GeV/c, and  $K^+p$  scattering at 50 GeV/c to evaluate the eikonals used in the present analysis, where  $A$  is in units of  $(\text{mb})^{1/2}(\text{GeV}/c)^{-1}$ , and  $t_1, t_2$ , and  $\lambda^2$  are in units of  $(\text{GeV}/c)^2$ .

Process	$p_L(\text{GeV}/c)$	$A$	$-t_1$	$-t_2$	$n$	$\lambda^2$	$\chi^2/N_{\text{DF}}$	Refs. of expts.	
								$d\sigma/dt$	$\rho$
$pp$	200	4.94	1.44	22.00	5.83	1.11	$\frac{227}{81}$	[23,24]	[26]
$\pi^-p$	200	3.11	3.53	20.00	4.77	1.03	$\frac{187}{84}$	[23,32]	[42]
$K^+p$	50	2.32	3.88	20.00	4.32	1.05	$\frac{26}{39}$	[23,31]	[44]

where  $K_n$  is the modified Bessel function of the order  $n$ .

Let the eikonal be  $\Omega(s_0, b)$  evaluated from the experimental data at  $s_0$  with the parametrization (11). Then it can be written as

$$\Omega(s_0, b) = \Omega_0(A, t_1, t_2, \lambda, n, \lambda b).$$

Since the eikonal in GGS is given by  $\Omega(s, b) = w(s)g(b/r(s))$ , Eq. (5), we identify

$$w(s_0) \equiv 1 \quad \text{and} \quad r(s_0) \equiv \frac{1}{\lambda}, \quad (13)$$

and use the eikonal given by

$$\Omega(s, b) = w(s)\Omega_0(A, t_1, t_2, \lambda, n, b/r(s)), \quad (14)$$

in the following analysis, where  $w(s)$  and  $r(s)$  are taken at each energy point  $s$  to reproduce the experimental values of the elasticity  $x$  and the total cross section  $\sigma_t$ .

We made a  $\chi^2$  minimization fit to the experimental data of differential cross sections of  $pp$  scattering at  $p_L=200$  GeV [23,24] with the form (11) for the imaginary part of the scattering amplitude and with the real part given by the Martin formula (4) with  $\rho = -0.02$  [26]. The obtained best-fit solution gives  $\sigma_t = 39.60$  mb and

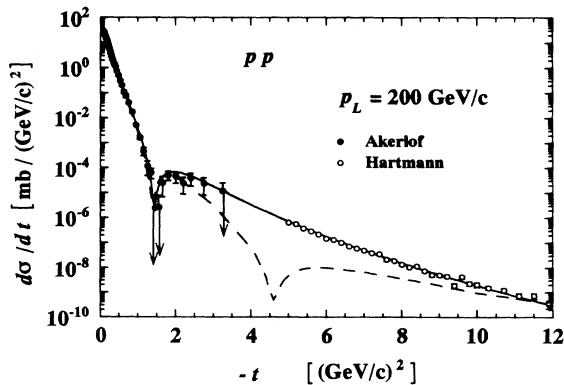


FIG. 1. The results of fit to the measured differential cross sections of  $pp$  scattering at  $p_L=200$  GeV/c [23,24] with the form of (11) for the imaginary part of the scattering amplitude (the solid curve). The real part is included in the fitting by taking the Martin formula (4) with  $\rho = -0.02$  [26]. The dashed curve corresponds to the “dipole” case giving the same total and elastic cross sections.

$\sigma_{\text{el}} = 7.08$  mb, while the empirical fit with formula

$$\sigma(p_L) = C_1 + C_2 p_L^n + C_3 \ln^2(p_L) + C_4 \ln(p_L)$$

to the total and elastic cross sections [27] gives 38.76 and 6.89 mb, respectively. For consistency with the empirical-formula value of  $\sigma_t = 38.76$  mb, we renormalize  $A$  by multiplying a factor  $(38.76/39.60) \approx 0.98$ . This is equivalent to a normalization factor  $(38.76/39.60)^2$  for the differential cross-section data, which may be allowed as the uncertainty in the normalization of the cross section around this energy, and gives  $\sigma_{\text{el}} = 6.79$  mb which is smaller than the empirical fit by 0.1 mb [28]. The solution after renormalization of  $A$  is given in Table I.

The fit of this solution to the measured differential cross sections is shown in Fig. 1 as well as the “dipole” one. The eikonals for  $\pi p$  and  $K p$  scattering were determined in a similar way as given later. We take the same eikonal function for both hadron-hadron and antihadron-hadron, since this is required to satisfy the asymptotic equivalence of two processes.

In Fig. 2, we show the eikonal  $\Omega(s, b) = \Omega(s_0, b)$  of  $pp$

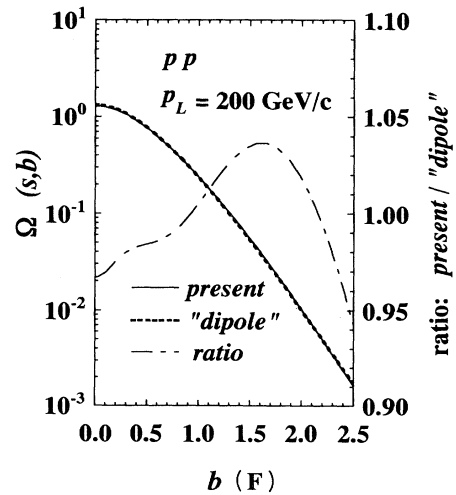


FIG. 2. The eikonal  $\Omega(s, b)$  of  $pp$  scattering at  $p_L=200$  GeV/c used in the present analysis (the solid curve) together with that of the “dipole” adjusted to the same total and elastic cross sections for the same value of  $\rho$  (the dashed curve). We also show the ratio of the present eikonal to the “dipole” one by the dot-dashed curve.

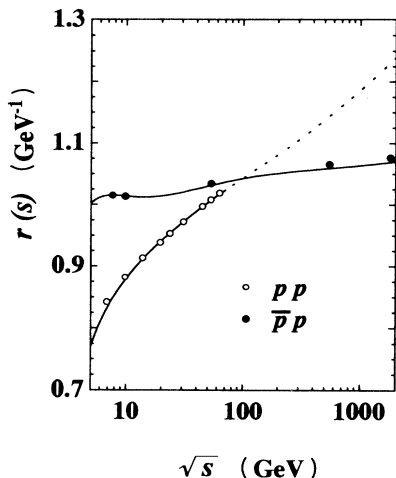


FIG. 3. The energy dependence of the scaling parameter  $r(s)$  is shown for  $pp$  (the open circles) and  $\bar{p}p$  (the solid circles) scattering taking with the values of the total and elastic cross sections given by the empirical fit [27]. These open and solid circles are evaluated at the experimental energy points discussed in this analysis by taking account of the real part of scattering amplitude, while the solid curves are calculated for vanishing real part. The dotted curve is the extrapolation using the empirical-fit formula for  $pp$  scattering.

scattering together with the “dipole” one evaluated at 200 GeV/c. In Fig. 3, we give the scaling length parameters  $r(s)$  of the present solution for the observed total and elastic cross-section data of  $pp$  and  $\bar{p}p$  scattering in the energy region  $5 \leq \sqrt{s} \leq 2000$  GeV. Here we have used the results of the empirical fit [27] as the experimental data of the total and elastic cross sections. The solid and dotted curves have been obtained by assuming  $\rho=0$ , while the open and solid circles have been evaluated by taking into account the real part, which increases the value of  $r$ . The difference of  $r(s)/r(s_0)$  between the present eikonal and the “dipole” becomes noticeable only above 2 TeV, but very small even there. The dependence of the strength function  $w(x_I(s), g)$  on the elasticity  $x_I$  is shown in Fig. 4 and on the energy for  $pp$  and  $\bar{p}p$  scatter-

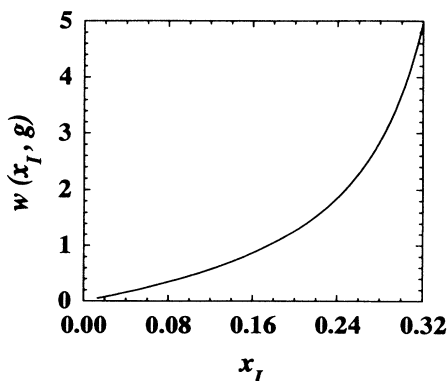


FIG. 4. Dependence of the strength function  $w(x_I(s), g)$  on the imaginary-part elasticity  $x_I$  for the present eikonal function of  $pp$  and  $\bar{p}p$  scattering.

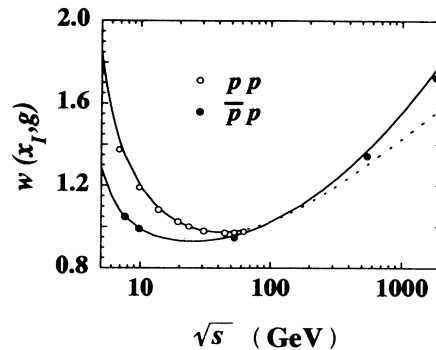


FIG. 5. Dependence of the strength function  $w(x_I(s), g)$  on the energy  $\sqrt{s}$  for the total and elastic cross sections of the empirical fit [27] of  $pp$  (the open circles) and  $\bar{p}p$  (the solid circles) scattering calculated for the present eikonal. These open and solid circles are evaluated by taking account of the real part of scattering amplitude at the experimental energy points discussed in this analysis, while the solid curves are calculated for vanishing real part. The dotted curve is the extrapolation using the empirical-fit formula for  $pp$  scattering.

ing cross-section data [27] in Fig. 5. In Fig. 5, we can see that the constancy of  $w(x_I(s), g)$  approximately holds only in the very limited regions around  $\sqrt{s} = 40$  GeV for  $pp$  and  $\sqrt{s} = 25$  GeV for  $\bar{p}p$ , where we could expect the GS behavior.

#### IV. COMPARISON WITH EXPERIMENTS

We compare the predictions of GGS mainly with the experimental data of differential cross sections of  $pp$  and  $\bar{p}p$  scattering. We also discuss  $\pi^+p$  and  $K^+p$  scattering, though their data are only available at *low* energies  $\sqrt{s} \leq 20$  GeV. In the present analysis we use the values of  $\sigma_t$  and  $\sigma_{el}$  of the fit with empirical formula [27] rather than the measured values at respective experimental points as the input data to the GGS calculation.

The results of GGS are sensitive to the input parameters in some aspects. For example, the change of  $\sigma_{el}$  of  $pp$  scattering by 1% at the ISR energy range produces change of  $\sim 10\%$  of the differential cross sections at the bump region, and, therefore, affects our *conclusions* on the validity of the GGS hypothesis. On the other hand, the determination of the basic eikonal may involve an uncertainty of about 0.1 mb for  $\sigma_{el}$  as was seen in the preceding section [28]. We fix  $\sigma_t$  at the value of the empirical formula, since  $\sigma_t$  is generally the most reliable among the input parameters, while  $\sigma_{el}$  will be varied around the value of the empirical formula and  $\rho$  around the dispersion-relation calculation or the measured one, when the predictions show deviations from experimental results.

##### A. $pp$ scattering

###### 1. CERN ISR region

If the elasticity  $x$  (more strictly,  $x_I$ ) is stationary with energy, GGS reduces to GS. At CERN ISR energies this

TABLE II. Input parameters used in the calculation of the differential cross sections by GGS. The values of  $\sigma_t$  and  $\sigma_{el}$  are those of the empirical fit [27]. The numerical figures marked with an asterisk are chosen to give a better fit to the experiments. See text.

Process	$\sqrt{s}$ (GeV)	$p_L$ (GeV/c)	$\sigma_t$ (mb)	$\sigma_{el}$ (mb)	$\rho$	Ref. of $\rho$	Shown in	
$pp$	19.4	200	38.76	6.79	-0.02	[26]	Fig. 1	
	23.5		39.23	6.87	0.02	[4]	Fig. 6	
	30.7		40.14	6.95	0.042	[4]	Fig. 6	
	44.7		41.92	7.22	0.062	[4]	Fig. 6	
	52.8		42.90	7.41	0.078	[4]	Fig. 6	
	62.5	44.01	7.63	0.095	[4]	Fig. 6		
	6.8	24	38.94	8.30	-0.20	[26]	Fig. 8	
			38.94	*8.70	-0.20		(Dotted)	
		9.8	50	38.35	7.49	-0.13	[26]	Fig. 8
		13.8	100	38.30	7.07	-0.10	[26]	Fig. 8
$\bar{p}p$	53		44.24	7.53	0.106	[26]	Fig. 9	
	546		61.35	12.80	*0.17		Fig. 10	
	1800		74.80	17.60	0.14	[39]	Fig. 11	
	7.6	30	46.13	8.31	-0.03	[26]	Fig. 12	
			*35.00	*6.50	-0.03	[26]	(Dotted)	
	9.8	50	44.03	7.67	-0.014	[26]	Fig. 12	
			*38.40	*6.80	-0.014	[26]	(Dotted)	
	40000		124	37	0.1		Fig. 18	

holds approximately around 40 GeV as seen in Fig. 5. Amaldi and Schubert have given  $x=0.1747\pm 0.0012$  in this energy range [4] in their critical survey, while the latest empirical fit [27] gives  $x=0.1752, 0.1730, 0.1722, 0.1726,$  and  $0.1734$  at  $\sqrt{s}=23.5, 30.7, 44.7, 52.8,$  and  $62.5$  GeV, respectively. Amaldi and Schubert concluded that GS holds reasonably well at the ISR energy range. See also Ref. [29].

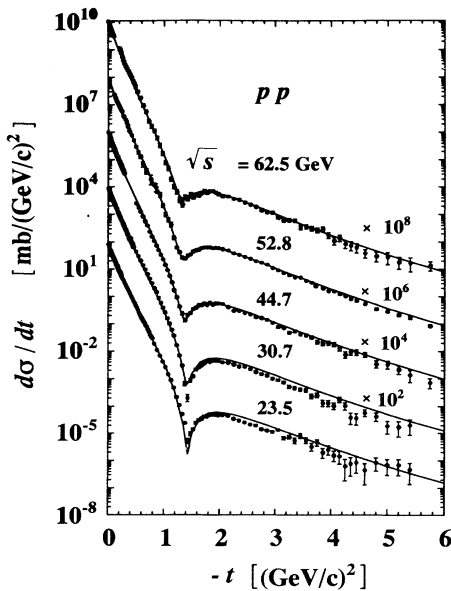


FIG. 6. Predictions of GGS for the differential cross sections of  $pp$  scattering at ISR energies. The results are shown at  $\sqrt{s}=23.5, 30.7, 44.7, 52.8,$  and  $62.5$  GeV together with the experimental data [13–20]. The values of  $\rho$  are taken from Ref. [4].

The input values of  $\sigma_t$ ,  $\sigma_{el}$ , and  $\rho$  are summarized in Table II. In Fig. 6, we give the present GGS predictions together with the experimental results [13–20]. They are in good agreement with the experiments at 44.7, 52.8, and 62.5 GeV. At 23.5 and 30.7 GeV we have found good agreement of the predictions with experiments except for that the predicted cross sections are larger by  $\sim 30\%$  than the measurements at and around  $-t=3$   $(\text{GeV}/c)^2$ . These discrepancies at 23.5 and 30.7 GeV seem somewhat large to attribute to the uncertainties in the normalization of measurements, unless some unknown systematic errors exist. By taking  $\sigma_{el}$  smaller by  $\sim 0.1$  mb from the empirical values at these energies, we can achieve some improvement in the fit to the experiments at the bump region, though not completely.

In Fig. 7, we compare the present solution with the

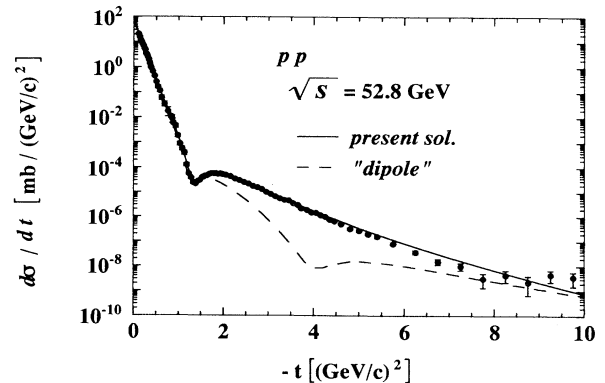


FIG. 7. The differential cross sections of  $pp$  scattering at  $\sqrt{s}=52.8$  GeV are given at the full range of momentum transfer of the experiments [19,20] for the present eikonal (the solid curve) as well as for the “dipole” one (the dashed curve).

predictions of the “dipole” at 52.8 GeV at the full  $t$  range of the momentum transfers of the measurements. The rapid departure of the “dipole” from the present solution and also from the experiments around from  $-t=1.5$   $(\text{GeV}/c)^2$  is observed.

There exists some small but systematic deviation of the GGS predictions from the experiments at large momentum transfers  $-t \geq 5$   $(\text{GeV}/c)^2$ , which may indicate either that the energy point with  $p_L=200$   $\text{GeV}/c$  is not fully in the GGS regime or that GGS is becoming weakly violated as the momentum transfer increases.

## 2. Below CERN ISR

Although GGS or GS may be likely to be realized at high energies, it is interesting to see to what extent the GGS structure appears at sub-ISR energies. In order to examine this, however, we have to separate out nondiffractive components which become dominant as the energy goes down. This involves considerable uncertainties. Here we give the simple predictions of GGS at  $p_L(\sqrt{s})=24$  (6.8), 50 (9.8), and 100 (13.8)  $\text{GeV}/c$  ( $\text{GeV}$ ) together with the experimental data [23,30–32] in Fig. 8, expecting that nondiffractive components to the imaginary part may not be so large in the exotic  $pp$  channel. The results at 50 and 100  $\text{GeV}/c$  are consistent with such an expectation, showing reasonable agreement with experiments. The elasticity at 50  $\text{GeV}/c$  is 0.195 which is about 10% larger than those in the ISR region and clearly indicates that this energy point is out of the ISR GS region.

Even at 24  $\text{GeV}/c$  we can have a good agreement with the measured data [30], if we take  $\sigma_{\text{el}}=8.70$  mb instead of the value of the empirical formula 8.30 mb, while

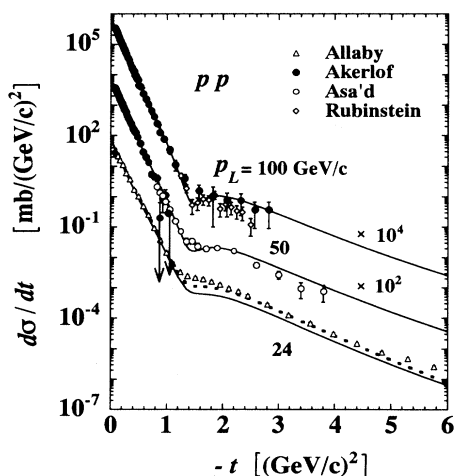


FIG. 8. Comparison of GGS with the experiments of  $pp$  scattering below ISR energies. We show the predictions at  $p_L=24$ , 50, and 100  $\text{GeV}/c$  together with the experiments; Akerlof [23], Allaby [30], Asa'd [31], and Rubinstein [32]. The solid curves are the GGS calculations for the  $\sigma_t$  and  $\sigma_{\text{el}}$  of the empirical fit [27]. The real parts are taken from Ref. [26]. The dotted curve at 24  $\text{GeV}/c$  is obtained for  $\sigma_{\text{el}}=8.70$  mb, keeping other parameters at the same values.

keeping  $\sigma_t$  at that of the empirical fit. See the dotted curve in Fig. 8. This value of  $\sigma_{\text{el}}$  seems still within the uncertainty of the present experimental data. If such a value of  $\sigma_{\text{el}}$  is excluded experimentally, we will need a smaller  $\sigma_t$ , which may lead to the necessity of nonscaling components.

## B. $\bar{p}p$ scattering

### 1. CERN ISR region

In this region the elasticity of  $\bar{p}p$  interaction is weakly increasing with energy. The scaling length parameter  $r(s)$  calculated from the cross sections of the empirical fit seems to follow the curve  $\sqrt{\sigma_t}/x_I$  [6,33] rather than the geometrical one  $\sqrt{\sigma_t}$ , exposing some sensitivity of  $r(s)$  to  $x_I$ . As shown in Fig. 5, the GS behavior might be observed around 25 GeV and the GGS effects will be more noticeable than in  $pp$  scattering at 25–60 GeV. Unfortunately, however, there are no data accurate enough to examine this point. The  $pp$  eikonal determined at 200  $\text{GeV}/c$  predicts the  $\bar{p}p$  differential cross sections at 53 GeV as shown in Fig. 9 for  $\sigma_t=44.24$  mb and  $\sigma_{\text{el}}=7.53$  mb of the empirical fit [27] and  $\rho=0.106$  of the measurement [26]. The agreement of GGS with the experiments [20,34] is reasonable. A better agreement in the dip region is attained if a slightly larger value of  $\rho$ , say 0.12, is assumed.

### 2. Above CERN ISR

Next we see what happens at CERN- $S\bar{p}p$ S and Fermilab Tevatron energies. The elasticity  $\chi(s)$  starts increasing markedly as the energy goes above the range covered by ISR. This leads to slower increasing of the scaling pa-

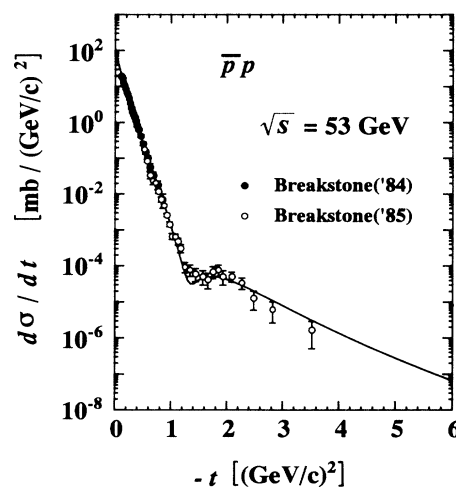


FIG. 9. The differential cross sections of  $\bar{p}p$  scattering calculated by GGS at  $\sqrt{s}=53$  GeV from the eikonal determined from  $pp$  scattering at  $p_L=200$   $\text{GeV}/c$  together with the experimental data, Breakstone [20] and Breakstone [34]. Here we have taken  $\sigma_t$  and  $\sigma_{\text{el}}$  of the empirical fit [27], and  $\rho$  of the measurement [26].

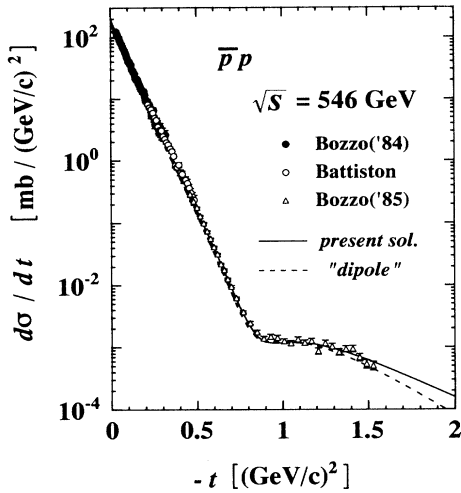


FIG. 10. The predicted differential cross sections of  $\bar{p}p$  scattering at 546 GeV by GGS (the solid curve) together with the measured ones, Bozzo (1984), Battiston, and Bozzo (1985) [21], while the dashed curve is for the “dipole.” Here we have taken  $\rho=0.17$  for both cases.

parameter  $r(s)$  with increasing  $\sigma_t$ , as shown in Fig. 3. Some FE-type effects [35] are then induced by the slow change of  $r(s)$  in this energy region.

The differential cross sections at 546 GeV calculated by GGS are shown in Fig. 10. The predictions are in good agreement with the experiments [21]. Here  $\rho$  is taken to be 0.17, which should be compared with 0.13 of the dispersion-relation calculation [36] and 0.24 of the measurement [37]. In order to obtain a good agreement with the experiments around  $-t=0.8$  (GeV/c)<sup>2</sup>, a value 0.16–0.2 is preferred, but a value as large as the measured one 0.24 is not favored. We note that there may be a correction to the Martin formula. Such a correction

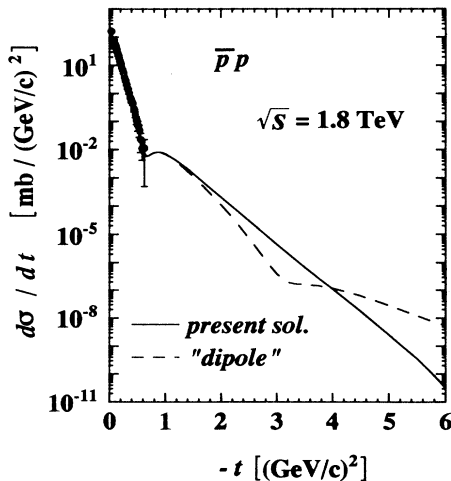


FIG. 11. The differential cross sections at  $\sqrt{s}=1.8$  TeV of  $\bar{p}p$  scattering calculated by GGS for the present eikonal (the solid curve) and for the “dipole” eikonal (the dashed curve) together with the experimental data [22].

amounts to be 33% at the dip position, if we take the calculation of Henzi and Valin [38]. This gives an enhancement by a factor 1.5 at the dip which implies  $\rho=0.13$  of the dispersion relation effectively as large as  $\sim 0.2$ . In order to discuss the workability of the Martin formula, we need a more accurate value of  $\rho$ .

The results of the calculation at 1.8 TeV are given in Fig. 11 and fit well the measurements [22]. Here we have taken the real part with  $\rho=0.14$  [39]. The concave curvature structure seems to practically disappear at  $-t=0-0.3$  (GeV/c)<sup>2</sup> consistently with the experimental data [40].

Here it should be emphasized that the present experimental data at  $Spp\bar{p}S$  and Tevatron cannot reject the possibility that the form of the eikonal determined at 200 GeV/c is gradually changing into the “dipole” or any other form at higher energies. It is essential to carry out the experiment at momentum transfers  $-t \geq 4$  (GeV/c)<sup>2</sup> in the  $Spp\bar{p}S$  Tevatron energies for confirmation of the GGS behavior.

### 3. Below CERN ISR

As the energy goes down from ISR we certainly have increasing contributions from nondiffractive components, which are expected to be larger than in exotic  $pp$  scattering. Therefore, without suitable evaluation of these effects, it may not be possible to discuss GGS properly. Here we first give naive predictions at  $p_L(\sqrt{s})=30$  (7.6) and 50 (9.8) GeV/c (GeV), without making any consideration on nondiffractive contributions. The results are given by the solid curves in Fig. 12.

At 30 GeV/c the agreement with the experiment [31] is

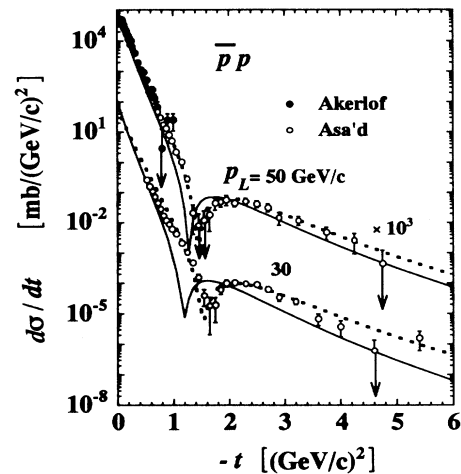


FIG. 12. Predictions of GGS for  $\bar{p}p$  scattering below ISR energies. The solid curves are the calculations at  $p_L=30$  and 50 GeV/c for the total and elastic cross sections of the empirical fit [27], while the dotted ones are those for the values of  $\sigma_t$  and  $\sigma_{el}$  tentatively taken to reproduce the dip-bump region,  $(\sigma_t, \sigma_{el})=(35.00, 6.50)$  mb at 30 GeV/c and  $(38.40, 6.80)$  mb at 50 GeV/c. The experimental data of differential cross section are Akerlof [23] and Asa'd [31]. Here we have taken the dispersion-relation values for  $\rho$  [26].

very poor, but at 50 GeV/c the predictions approach the measurements [23,31], though some discrepancy still remains. This situation is very different from the case of  $pp$  scattering. The important fact is, as emphasized by many authors, that the movement of the dip with energy, which is primarily determined by the change of the total cross section in the geometrical model, is just the opposite between the GGS (GS) implication and the experiments.

Kroll [29] suggested that GS would hold even at 50 GeV/c, if suitable nondiffractive components were taken into account. In this spirit we try to fit the cross sections at the dip-bump region by taking effective  $\sigma_t$  and  $\sigma_{el}$ . We give the results of some attempts: the dotted curves in Fig. 12 correspond to the cases with  $(\sigma_t, \sigma_{el}) = (35.00, 6.50)$  mb at 30 GeV/c and  $(38.40, 6.80)$  mb at 50 GeV/c. These examples are not the results of the best-fit search, but are taken tentatively to obtain some idea about the possible sizes of the diffractive components involved in the measured values of  $(\sigma_t, \sigma_{el}) = (46.13, 8.31)$  mb at 30 GeV/c and  $(44.03, 7.67)$  mb at 50 GeV/c, if the GGS behavior is kept. These examples together with the results of  $pp$  scattering suggest that the diffraction component seems to retain the GGS property even below ISR region down to nearly 10 GeV.

### C. $\pi p$ and $Kp$ scattering

The meson-nucleon scattering differential cross-section data are only available at  $p_L(\sqrt{s}) \leq 200$  GeV/c (20 GeV). The experimental data of differential cross sections are found in Refs. [23,31,32] and we use the values of  $\rho$  of the measurements or the dispersion-relation fit in [41–44]. We proceed the analysis in the same way as done for  $pp$  and  $\bar{p}p$  scattering. An immediate question will be whether the form of the  $pp$  eikonal can well describe meson-baryon scattering. The answer is negative. Also  $\pi p$  and  $Kp$  cannot be described by the same eikonal.

### 1. $\pi p$ scattering

The starting eikonal was determined by  $\pi^-p$  scattering data at  $p_L = 200$  GeV/c [23,32] using the same functional form (11) for the imaginary part of the scattering amplitude. The resultant amplitudes gave  $\sigma_t = 23.84$  and  $\sigma_{el} = 3.18$  mb, which should be compared with the empirical fit values  $\sigma_t = 24.46$  and  $\sigma_{el} = 3.34$  mb. As in the case of  $pp$  scattering renormalization of  $A$  gives  $\sigma_{el} = 3.35$  mb. The final results after renormalization are given in Table I. The fit of this solution to the experiments is shown in Fig. 13.

The predictions of  $\pi^-p$  and  $\pi^+p$  scattering are shown in Figs. 14 and 15. The input values of  $\sigma_t$ ,  $\sigma_{el}$ , and  $\rho$  are summarized in Table III.

The results for  $\pi^-p$  scattering are in good agreement with measurements at  $p_L = 50$  [23,31] and 100 [23,32] GeV/c in the region  $-t \leq 2.5$  (GeV/c)<sup>2</sup> and reasonable at  $-t \geq 4.5$  (GeV/c)<sup>2</sup>. Between these two regions the agreement is poor: GGS predicts a sharp dip structure with the observed value of  $\rho$ , but the experiments show no clear indication at 50 GeV/c.

The experimental data of  $\pi^+p$  [23,31,32] are systematically below the GGS predictions at 100 and 200 GeV/c in the forward peak region, though the shapes of the differential cross section are quite alike. We suspect that these discrepancies are due to inconsistency among the present input values of  $\sigma_t$ ,  $\sigma_{el}$ , and the measured differential cross sections, rather than the failure of GGS. At 50 GeV/c the predictions of GGS reproduce well the data at small and large  $-t$ . We again see discrepancy in the dip region at 50 GeV/c, though not bad as in the case of  $\pi^-p$ .

The observed discrepancies around  $-t = 2.5 - 4.5$  (GeV/c)<sup>2</sup> both in  $\pi^-p$  and  $\pi^+p$  scattering seem to come from the real part of the scattering amplitude. We have tentatively tried to fit the experimental data by taking an effective value of  $\rho$ , under the assumption that Martin's formula holds locally around the dip. The results are given in Figs. 14 and 15 by the dotted curves, which

TABLE III. Input parameters used in the calculation of the differential cross sections by GGS. The values of  $\sigma_t$  and  $\sigma_{el}$  are those of the empirical fit [27]. The numerical figures marked with an asterisk are chosen to give better fit to the experiments. See text.

Process	$\sqrt{s}$ (GeV)	$p_L$ (GeV/c)	$\sigma_t$ (mb)	$\sigma_{el}$ (mb)	$\rho$	Ref. of $\rho$	Shown in
$\pi^-p$	9.7	50	24.28	3.33	-0.003	[41]	Fig. 14
			24.28	*3.48	*0.15		(Dotted)
	13.7	100	24.14	3.26	0.048	[42]	Fig. 14
$\pi^+p$	19.4	200	24.46	*3.35	0.064	[42]	Fig. 13
	9.7	50	23.04	3.59	-0.06	[43]	Fig. 15
			23.04	3.59	*0.20		(Dotted)
$K^+p$	13.7	100	23.22	3.48	-0.003	[43]	Fig. 15
	19.4	200	23.82	3.59	0.053	[43]	Fig. 15
	9.7	50	18.17	*2.14	-0.028	[44]	Fig. 16
$K^-p$	13.7	100	19.01	2.41	0.065	[43]	Fig. 16
	19.4	200	20.10	2.60	0.071	[43]	Fig. 16
	9.7	50	20.29	2.35	0.1	[43]	Fig. 17
	13.7	100	20.31	2.40	0.12	[43]	Fig. 17
	19.4	200	20.96	2.72	0.161	[43]	Fig. 17

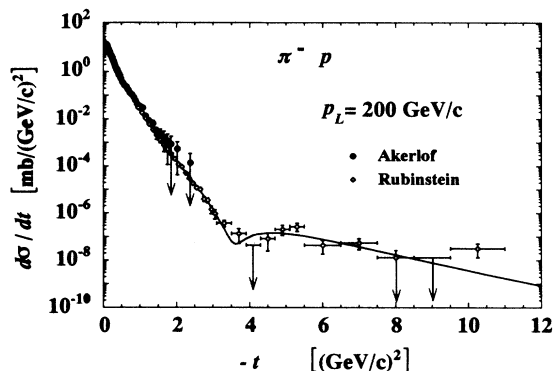


FIG. 13. Comparison of the solution obtained by fitting to the measured differential cross section of  $\pi^-p$  scattering at  $p_L=200$  GeV/c with the experimental data; Akerlof [23] and Rubinstein [32]. The value of  $\rho$  has been taken from [42].

show, unlike the case of  $\bar{p}p$  case, the discrepancy may primarily be reduced to the real part.

## 2. $Kp$ scattering

Since the experiment extending to large momentum transfers was performed only at 50 GeV/c [31], we determined the basic eikonal from the experimental data of  $K^+p$  scattering at this energy. This may be allowable as the process is exotic. The resultant amplitude gives  $\sigma_t=19.99$  mb and renormalization of  $A$  to get  $\sigma_t=18.17$  mb of the empirical fit leads to the parameters shown in Table I. The fit of this solution to the experiments is shown in Fig. 16. We have  $\sigma_{el}=2.14$  mb, which is com-

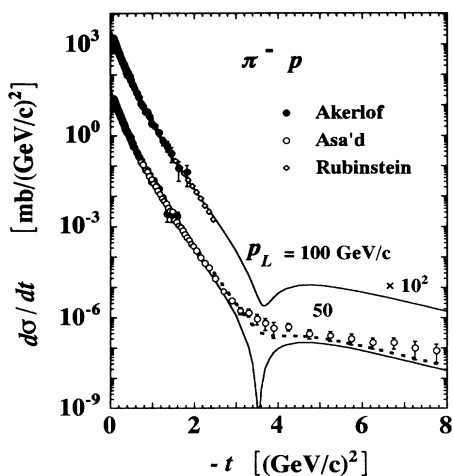


FIG. 14. Predictions of GGS for  $\pi^-p$  scattering at  $p_L=50$  and 100 GeV/c. The solid curves are the calculations with the total and elastic cross sections of the empirical fit [27] and the values of  $\rho$  from [41,42], while the dotted one at 50 GeV/c is that for  $\sigma_{el}=3.48$  mb and  $\rho=0.15$  tentatively taken to reproduce the dip-bump region. The experimental data of the differential cross section are taken from Akerlof [23], Asa'd [31], and Rubinstein [32].

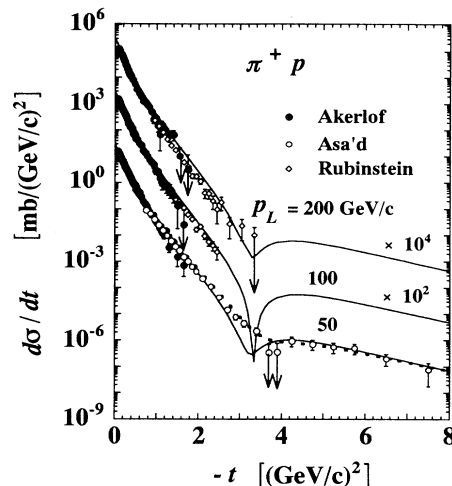


FIG. 15. Predictions of GGS for  $\pi^+p$  scattering at  $p_L=50$ , 100, and 200 GeV/c. The solid curves are the calculations with the total and elastic cross sections of the empirical fit [27] with the values of  $\rho$  of the dispersion-relation fit at 50 GeV/c and of the measurements at 100 and 200 GeV/c [43], while the dotted one at 50 GeV/c is that of  $\rho=0.2$  tentatively taken to reproduce the dip-bump region. The experimental data of the differential cross section are taken from Akerlof [23], Asa'd [31], and Rubinstein [32].

pared with 2.37 mb of the empirical fit and  $2.27 \pm 0.09 \pm 0.05$  mb of the measurement [45]. The predictions for  $K^+p$  scattering at 100 and 200 GeV/c are shown in Fig. 16 and for  $K^-p$  scattering at 50, 100, and 200 GeV/c in Fig. 17. The input values of  $\sigma_t$ ,  $\sigma_{el}$ , and  $\rho$  used in the calculation are given in Table III. These

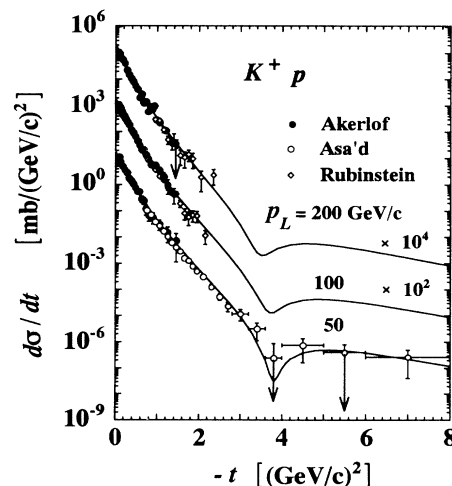


FIG. 16. Predictions of GGS for  $K^+p$  scattering at  $p_L=100$  and 200 GeV/c and also the result of fitting at 50 GeV/c which is used to determine the eikonal. The solid curves are the calculations for the total and elastic cross sections of the empirical fit [27] and the values of  $\rho$  of the measurements [43,44]. The experimental data of the differential cross section are taken from Akerlof [23], Asa'd [31], and Rubinstein [32].

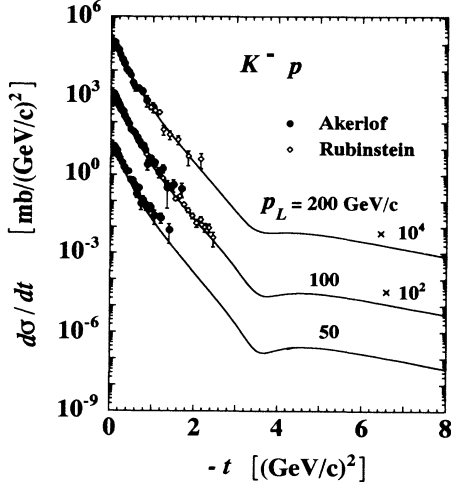


FIG. 17. Predictions of GGS for  $K^-p$  scattering at  $p_L = 50, 100,$  and  $200$  GeV/c. The solid curves are the calculations with the total and elastic cross sections of the empirical fit [27] and the values of  $\rho$  of the dispersion relation fit at 50 and 100 GeV/c and of the measurement at 200 GeV/c [43]. The experimental data of the differential cross sections are taken from Akerlof [23] and Rubinstein [32].

figures show that the theoretical predictions are in good agreement with the measurements [23,31,32], though they are available mostly at small momentum transfers,  $-t \leq 2.5$  (GeV/c)<sup>2</sup>.

### V. SUPERCONDUCTING SUPER COLLIDER REGION

In order to see what can be expected at the energy range aimed for by the Superconducting Super Collider (SSC), we have calculated the differential cross sections of  $\bar{p}p$  scattering at  $\sqrt{s} = 40$  TeV by taking the total and elastic cross sections of the empirical fit [27] as the input data. We also give the results for the “dipole” eikonal for comparison. The results are shown in Fig. 18.

In both cases we tentatively have assumed  $\rho = 0.1$ . Two are practically the same up to  $-t = 1.5$  (GeV/c)<sup>2</sup> with the exhibiting downward curvature structure of the forward peak; the difference between two distributions is not large even beyond this point. Therefore, the distinction between the present solution and the “dipole” seems practically unfeasible at 40 TeV, unless we perform the measurements beyond  $-t = 4$  (GeV/c)<sup>2</sup>.

Here we comment on the possibility of many dips at high energies as the total cross section gets higher. The appearance of many dips is almost inherent to the geometrical models including the present one. The positions of dips are naturally closely related with the shape of the eikonal. At 200 GeV/c the position of the second dip is  $-t_2 = 22$  (GeV/c)<sup>2</sup>, while the “dipole” gives at 4 (GeV/c)<sup>2</sup>. At 40 TeV, these second dips move nearly to the same position around  $-t = 1.5$  (GeV/c)<sup>2</sup>. The same situation will occur for the third and successive dips as the total cross section and the elasticity increase.

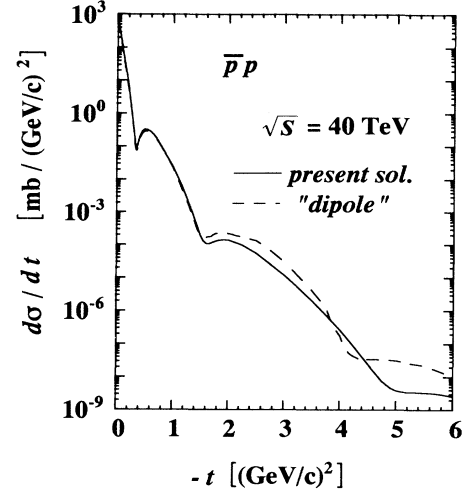


FIG. 18. The calculated differential cross section of  $\bar{p}p$  scattering by GGS at  $\sqrt{s} = 40$  TeV. The input data are  $\sigma_t = 124$  and  $\sigma_{el} = 37$  mb obtained by extrapolating the empirical fit to the experiments below 2 TeV [27]. The value of  $\rho$  is assumed to be 0.1. The solid curve is for the present eikonal while the dashed curve is for the “dipole.”

Finally, if the total cross section rises indefinitely with increasing energy and the elasticity approaches a finite limit asymptotically, then the GS structure will appear, consistently with the general theorem [3].

### VI. COMMENT ON THE EIKONAL

The Fourier-Bessel transform of the eikonal to the momentum-transfer representation is given by

$$\bar{\Omega}(s, t) = \int_0^\infty b db J_0(b\sqrt{-t}) \Omega(s, b). \quad (15)$$

In Fig. 19, we give the ratio of  $\bar{\Omega}(s, t)$  of the present solution of  $pp$  scattering to that of the “dipole,” both evaluated at  $p_L = 200$  GeV/c.

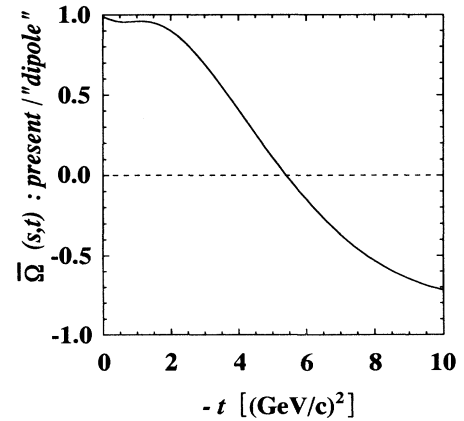


FIG. 19. The ratio of the transformed eikonal  $\bar{\Omega}(s, t)$  of the present solution of  $pp$  scattering to that of the “dipole” evaluated at  $p_L = 200$  GeV/c.

The transformed eikonal  $\bar{\Omega}(s, t)$  is negative in some region of  $t$ . If the eikonal is given by the convolution of two distributions, the transformed eikonal should be factorized and be positive definite. In order to obtain the positive definite transformed eikonal, the second dip is needed to be located at a smaller  $-t$ , say  $8 \text{ (GeV}/c)^2$  [25], which gives a somewhat poor fit to the present experiments of  $pp$  at large momentum transfers near and beyond the dip. A final conclusion for the existence of the zero in the transformed eikonal needs reliable information of the real part of the scattering amplitude at large momentum transfers, however.

## VII. CONCLUSIONS

(1) By taking the eikonal which fits the  $pp$  scattering data at  $p_L = 200 \text{ GeV}/c$  ( $\sqrt{s} = 19.4 \text{ GeV}$ ), we have shown that the generalized geometrical scaling hypothesis gives a reasonable interpretation of the behaviors of both  $pp$  and  $\bar{p}p$  differential cross sections over a wide energy range from ISR to Tevatron where the total energy varies by a factor  $10^2$  and the total cross section increases over 50%. Even below ISR energies we can see that GGS seems to be consistent with the measurements of  $pp$  scattering down to near  $10 \text{ GeV}$ .

(2) The GGS hypothesis has been tested also about  $\pi^\pm p$  and  $K^\pm p$  scattering. The experimental information of these processes is, however, very limited: the data are

available only at energies  $p_L \leq 200 \text{ GeV}/c$ . In these processes we have obtained reasonable agreement with the measurements, even at  $p_L = 50 \text{ GeV}/c$  except around the dip where the real part may be dominant and the Martin prescription (4) is found to be inappropriate.

(3) It will be necessary to stress the importance of performing experiments at large momentum transfers in the  $Spp\bar{S}$  Tevatron energy region. As shown in Fig. 18, the difference becomes small at SSC energies between the present eikonal which covers the whole  $-t$  region of the ISR experiments and the GGS scaled "dipole" which only reproduces the measurements up to the dip, while at  $Spp\bar{S}$  Tevatron energies the difference is still large, if the measurement can be extended up to around  $-t = 4 \text{ (GeV}/c)^2$  as shown in Fig. 11. Therefore, the experiment at this energy region is essential to test the proposed generalized geometrical scaling behavior at large momentum transfers. Our optimistic conclusion is that the GGS hypothesis for the imaginary part of the scattering amplitude seems to work reasonably well for all elastic processes tested at energies  $\sqrt{s} \geq 10 \text{ GeV}$ .

*Note added.* Recently a new value of  $\rho = 0.135 \pm 0.015$  measured at  $\sqrt{s} = 541 \text{ GeV}$  has been reported [46].

## ACKNOWLEDGMENTS

The numerical computations were carried out at the computer centers at Gifu University and Hiroshima University.

- 
- [1] J. Dias de Deus, Nucl. Phys. **B59**, 231 (1973); A. J. Buras and J. Dias de Deus, *ibid.* **B71**, 481 (1974).
  - [2] Z. Koba, H. B. Nielsen, and P. Olesen, Nucl. Phys. **B40**, 317 (1972).
  - [3] G. Auberson, T. Kinoshita, and A. Martin, Phys. Rev. D **3**, 3185 (1971).
  - [4] U. Amaldi and K. R. Schubert, Nucl. Phys. **B166**, 301 (1980).
  - [5] UA4 Collaboration, M. Bozzo *et al.*, Phys. Lett. **147B**, 392 (1984).
  - [6] M. Kawasaki, T. Maehara, and M. Yonezawa, Phys. Rev. D **47**, R3 (1993). After the completion of this work, the authors noticed the paper by V. Barger, J. Luthe, and R. J. N. Phillips, Nucl. Phys. **B88**, 237 (1975), which suggested the same generalization for geometrical scaling. See also T. T. Chou and C. N. Yang, Phys. Lett. B **244**, 113 (1990).
  - [7] T. T. Chou and C. N. Yang, Phys. Rev. **170**, 1591 (1968).
  - [8] L. Durand III and R. Lipes, Phys. Rev. Lett. **20**, 637 (1968).
  - [9] H. Cheng, J. K. Walker, and T. T. Wu, Phys. Lett. **44B**, 97 (1973); F. Hayot and U. P. Sukhatme, Phys. Rev. D **10**, 2183 (1974).
  - [10] A. Martin, Lett. Nuovo Cimento **7**, 811 (1973).
  - [11] R. Henzi, Nucl. Phys. **B104**, 52 (1976).
  - [12] The contribution to  $\sigma_{el}$  from the real part given by Eq. (4) is well approximated, numerically, by  $\frac{1}{2}\rho^2\sigma_{el}^I$  for the imaginary part used in the present analysis.
  - [13] G. Barbiellini *et al.*, Phys. Lett. **39B**, 663 (1972).
  - [14] A. Boehm *et al.*, Phys. Lett. **49B**, 491 (1974).
  - [15] N. Kwak *et al.*, Phys. Lett. **58B**, 233 (1975).
  - [16] M. G. Albrow *et al.*, Nucl. Phys. **B108**, 1 (1976).
  - [17] U. Amaldi *et al.*, Phys. Lett. **66B**, 390 (1977).
  - [18] L. Baksay *et al.*, Nucl. Phys. **B141**, 1 (1978).
  - [19] E. Nagy *et al.*, Nucl. Phys. **B150**, 221 (1979).
  - [20] A. Breakstone *et al.*, Nucl. Phys. **B248**, 253 (1984).
  - [21] UA4 Collaboration, R. Battiston *et al.*, Phys. Lett. **127B**, 472 (1983); UA4 Collaboration, M. Bozzo *et al.*, *ibid.* **147B**, 385 (1984); **155B**, 197 (1985).
  - [22] E-710 Collaboration, N. A. Amos *et al.*, Phys. Lett. B **247**, 127 (1990).
  - [23] C. W. Akerlof *et al.*, Phys. Rev. D **14**, 2864 (1976).
  - [24] J. L. Hartmann *et al.*, Phys. Rev. Lett. **39**, 975 (1977).
  - [25] T. Maehara, T. Yanagida, and M. Yonezawa, Prog. Theor. Phys. **57**, 1097 (1977).
  - [26] N. Amos *et al.*, Nucl. Phys. **B262**, 689 (1985). Also the values of  $\rho$  at some energy points were read from Fig. 11 in this reference.
  - [27] Particle Data Group, K. Hikasa *et al.*, Phys. Rev. D **45**, S1 (1992), p. III.83; see also *Total Cross Sections for Reactions of High Energy Particles*, edited by H. Schopper, Landolt-Börnstein, New Series Vols. I/12a and I/12b (Springer-Verlag, New York, 1988).
  - [28] Another way to achieve the consistency with the value of  $\sigma_t$  of the empirical formula is to calculate the eikonal, without renormalization of  $A$ , from the amplitude obtained by the  $\chi^2$  fit, and then to search for  $\sigma_{el}$  which reproduces the differential cross-section data by the GGS procedure with the empirical-fit value of  $\sigma_t$ . This is given by  $\sigma_{el} \approx 6.94 \text{ mb}$ , which is compared with  $6.89 \text{ mb}$  of the empirical formula and the measured value  $6.95 \pm 0.08 \text{ mb}$

- of V. D. Bartenev *et al.*, *Yad. Fiz.* **22**, 317 (1975) [*Sov. J. Nucl. Phys.* **22**, 164 (1975)]. This procedure results in only slightly different form of the eikonal, but the conclusion of the present analysis is essentially unchanged.
- [29] P. Kroll, *Z. Phys. C* **15**, 67 (1982).
- [30] J. V. Allaby *et al.*, *Nucl. Phys.* **B52**, 316 (1973).
- [31] Z. Asa'd *et al.*, *Nucl. Phys.* **B255**, 273 (1985).
- [32] R. Rubinstein *et al.*, *Phys. Rev. D* **30**, 1413 (1984).
- [33] The scaling with variable  $\sigma_1/x$  was suggested previously from the study of unitarity bounds, M. Kawasaki, T. Takaiishi, and M. Yonezawa, *Phys. Rev. Lett.* **67**, 1197 (1991).
- [34] A. Breakstone *et al.*, *Phys. Rev. Lett.* **54**, 2180 (1985).
- [35] For some aspects of FE, see the review article by M. M. Block and R. N. Cahn, *Rev. Mod. Phys.* **57**, 563 (1985).
- [36] This value was read from the curve by M. M. Block *et al.* given in Fig. 4 of Ref. [39].
- [37] D. Bernard *et al.*, *Phys. Lett. B* **198**, 583 (1987).
- [38] R. Henzi and P. Valin, *Phys. Lett.* **149B**, 239 (1984).
- [39] E-710 Collaboration, N. A. Amos *et al.*, *Phys. Rev. Lett.* **68**, 2433 (1992).
- [40] M. Kawasaki, T. Maehara, and M. Yonezawa, *Mod. Phys. Lett. A* **7**, 1905 (1992).
- [41] J. P. Burq *et al.*, *Phys. Lett.* **77B**, 438 (1978).
- [42] J. P. Burq *et al.*, *Phys. Lett.* **109B**, 111 (1982).
- [43] L. A. Fajardo *et al.*, *Phys. Rev. D* **24**, 46 (1981).
- [44] V. D. Akopin *et al.*, *Yad. Fiz.* **25**, 94 (1977) [*Sov. J. Nucl. Phys.* **25**, 51 (1977)].
- [45] D. S. Ayres *et al.*, *Phys. Rev. D* **15**, 3105 (1977).
- [46] UA4/2 Collaboration, C. Augier *et al.*, CERN Report No. CERN/PPE 93-115 (unpublished).